Journal of The Electrochemical Society, 2020 **167** 130508

Fast Charging of Li-Ion Cells: Part IV. Temperature Effects and "Safe Lines" to Avoid Lithium Plating

Marco-Tulio F. Rodrigues,[1] Ilya A. Shkrob,[1] Andrew M. Colclasure,[2] and Daniel P. Abraham[1,*,z]

[1]*Chemical Sciences and Engineering Division, Argonne National Laboratory, Lemont, Illinois, 60439, United States of America*
[2]*Center for Integrated Mobility Sciences, National Renewable Energy Laboratory, Golden, Colorado 80401, United States of America*

Fast charging of lithium-ion batteries that does not compromise cell performance and durability is critical for wider adoption of electric vehicles. Raising cell temperature is one approach to enable fast charge; the higher temperature facilitates charge migration and lowers electrode polarization limited by the rates of diffusion and interfacial transport. In this study we examine the behavior of cells subjected to constant current and pulse current charging, at rates from 1C to 8C in the 30 °C to 55 °C range. To demonstrate *safe* charge conditions that averts Li metal plating on the anode, we use a microprobe reference electrode to continuously monitor the electrode potentials during tests. We then adopt a state-of-the-art multiphase electrochemical model to extrapolate the anode *reference* potential to the anode *surface* potential, which determines the overpotential for Li plating. For constant current charging, the results suggest that safe charging at 6C to 80% full capacity would be untenable for all but the thinnest electrodes. For pulse charging, the *safe* conditions depend on cell voltage, temperature, and the rate/duration of the pulse. The "safe lines" established in this study can help define charging protocols that enable higher charge rates, while minimizing losses in cell performance over time.

 [DOI: 10.1149/1945-7111/abb70d]

Manuscript submitted July 23, 2020; revised manuscript received August 23, 2020. Published September 22, 2020.

Supplementary material for this article is available online

State-of-the-art high energy lithium-ion batteries (LIBs) with a layered oxide cathode and graphite anode can be charged at rates below 1C with little deterioration of cell performance (here 1C is equivalent to full discharge of a cell in an hour).[1,2] Charging at higher rates increases the likelihood of energy and power degradation because of irreversible losses in Li^+ ion inventory and increased resistance in the cell.[3,4,5] The U.S. Department of Energy (DOE) has identified the slow charge of LIBs as a major obstacle for electric vehicles and is funding research on cell materials, electrode architectures and cycling protocols[5,6] that would enable 80% of full charge in <10 min. In this series,[7–9] we systematically explore the various effects of fast charge in Li-ion cells. Our studies are intended to spur development of LIB cells that can be charged at a 6C rate without sacrificing safety and durability.

One of the recognized complications in fast charging of LIBs is Li metal plating on the anode, which occurs when the electrode potential becomes so low that this reaction becomes competitive with Li^+ ion intercalation into the graphite.[10–13] Charging at higher temperatures can mitigate this plating, but at a price.[14] The higher temperature enhances diffusion in the electrolyte, Li^+ ion desolvation processes at the electrode, and transport across the interfaces.[15] However, higher operating temperatures can lead to electrolyte decomposition and dissolution of the solid electrode interphase (SEI), which results in additional electrolyte reduction reactions that immobilize Li^+ ions. Other parasitic reactions include transition metal dissolution, phase changes, and surface film growth in the oxide-cathode. Thus, there is a fine balance between benign and detrimental effects of the higher temperature. Limiting exposure to high temperatures during fast charge, by rapid preheating of the cell and subsequent discharge at ambient temperature, has been shown to suppress Li plating and extend cycle life.[16]

In this study, we examine the effects of elevated temperature on electrochemistry during continuous and pulsed fast charging. The electrode potentials are determined using a reference microelectrode made of a thin lithiated copper wire that minimally interferes with ionic currents in the cell.[7,8] Two types of experiments are described below. The first is capacity controlled constant current charging, in which the potentials (that include the cell voltage U, cathode potential ϕ_c, and anode potential ϕ_a) are followed as a function of lithiation capacity Q. The second is pulse charging, in which the current is interrupted when $\phi_a = 0$ in order to avoid Li plating on the graphite. In both types of experiments the cells rest after charge and relaxation kinetics of the potentials are obtained. Avoiding Li deposition on the anode is a key concern: we show how safe regimes of fast charging can be mapped without crossing into the Li plating zones, which can cause irreversible performance loss in the cell.

Additional figures and animations are provided as Supporting Information. When referenced in the main text, these materials have the designator "S", as in Fig. S1 (available online at stacks.iop.org/JES/167/130508/mmedia).

Experimental

Materials.—Cell electrodes were punched from laminates fabricated at the Cell Analysis, Modeling and Prototyping (CAMP) facility of Argonne National Laboratory. Copper and aluminum current collectors (10 and 20 μm thick, respectively) were used for the anode and cathode, respectively. The graphite (Gr, 91.8 wt% Superior Graphite SLC1506) and $Li_{1.03}(Ni_{0.5}Co_{0.2}Mn_{0.3})_{0.97}O_2$ (NCM523, 90 wt%, TODA America) electrodes were ~70 μm thick and 20.3 cm^2 in area, with porosities of 34.5% and 35.4%, respectively.[8] The electrode matrices contained a polymer binder for cohesion and carbon particles for enhancing electron conductance. The 1.2 M $LiPF_6$ in 3:7 w/w liquid mixture of ethylene carbonate and ethyl methyl carbonate electrolyte (Tomiyama, Inc.) and Celgard 2320 separators (20 μm thick, 40% porosity) were used for cell assembly. The reference electrode was a 25 μm thin round copper wire with an electrochemically-lithiated tip (2–3 mm in length) placed between two separators at the center of the round electrodes.[7] Figure 1 shows its location in the cell, and associated terms used in this study. The test temperature was maintained using heating plates and a controller that monitored a thermocouple inside the stainless steel cell housing.

*Electrochemical Society Member.
[z]E-mail: abraham@anl.gov

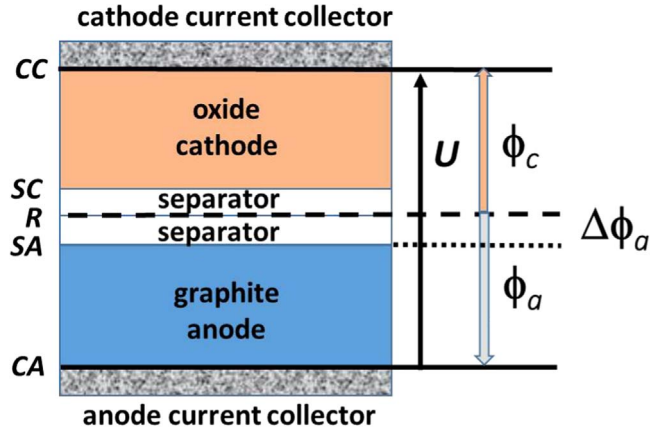

Figure 1. Schematic diagram of a Li-ion cell. ***CC*** is the oxide cathode current collector, ***CA*** is the graphite anode current collector, ***R*** is the reference electrode (measuring vs. Li/Li^+ redox potential) placed between two separators, ***SC*** and ***SA*** are the cathode and anode electrode surfaces, respectively, U is the cell voltage, $\phi_{a,c}$ are the anode and cathode reference potentials, respectively, and $\Delta\phi_a$ is the correction to obtain the anode surface potential η_a, which is also the Li plating overpotential.

Electrochemical cycling.—Cell assembly and testing was conducted inside an argon-atmosphere glove box. All cells underwent formation, consisting of two C/10 cycles and one C/25 cycle between 3.0 and 4.1 V. These NCM523//Gr cells display a discharge capacity Q_{full} of 2.4 mAh cm^{-2} when cycled slowly (~C/25 rate) between 3.0 and 4.1 V; the 1C rate was determined to be 1.97 mA cm^{-2}.

For the constant current tests (Fig. S1a) the cell was charged at a C-rate of 0.2, 1, 2, 3, 4, 5 and 6C to a specific capacity of 87 mAh g^{-1} (where g is grams of the fully-lithiated NCM523 oxide in the cathode). The charge limit was chosen so that at the highest rate of 6C the cell voltage U would be <4.4 V; cell deterioration occurs at higher voltages due to undesirable side reactions, such as electrolyte oxidation.[17,18] After every charge the cell rested at open circuit for 1 h and was then discharged at a C/5 rate to 3 V and held there until the current dropped below C/100. For the pulsed charge tests shown in Fig. S1b, the cell was equilibrated at ~3.57 V and rectangular current pulses (1C–8C) were applied in increments of 1C, in a random order. The pulse was either constant-capacity (2.5 mAh g^{-1}) or set for a time of 120 s; the actual pulse duration was often shorter due to the $\phi_a = 0$ termination condition. The cells rested (zero current) for 2 h after each pulse during which the data were acquired on a pseudo-logarithmic scale to better probe electrode relaxation kinetics. The cell was re-equilibrated at 3.57 V before every pulse; this cell voltage was selected to allow sufficient data collection before the pulse was interrupted at $\phi_a = 0$.

To examine cell performance degradation, capacity and impedance data were obtained at 30 °C, before and after the constant current and pulsed current tests at the set temperatures. The capacity measurements were from cells that were cycled at ~C/25 rate between 3 and 4.1 V. The area specific impedance (ASI) values were obtained using a modified version of the hybrid pulse power characterization (HPPC) test, which provides information over a range of electrode potentials and cell voltages.[19]

Electrochemical modeling.—To simulate the cell, we used the same electrochemical model that was used in our previous publications.[8] It is a Newman-style model in which the lithiated graphite is considered as a triphasic system consisting of the dilute, LiC_6, and LiC_{12} phases with the Avrami kinetic model used to explicitly treat the phase transitions[20]; here, the cathode is considered as a solid solution. The same model parameters were used as in Ref. 8, except for the exchange currents that were adjusted to obtain the correct C-rates at which ϕ_a becomes negative. The volume fractions of active materials in the graphite anode and oxide cathode are 59.4% and 50.4%, respectively, the active areas per unit volume are 26,912 and 6,612 cm^{-1}, respectively, and the theoretical maximum concentration of Li in these active materials are 30.5 M and 49.7 M, respectively. For the simulations, we assumed temperature independent diffusivity in the solid phases and adjusted the exchange currents to match experimental data. At 30 °C, the exchange currents for the electrodes were estimated to be 55 μA cm^{-2} for the cathode and 40 μA cm^{-2} for the anode, respectively; for 45 °C we estimated 55 μA cm^{-2} for the anode (the same exchange current is assumed for all three Li_xC_6 phases). At both temperatures, the initial cathode oxide lithium content was assumed to be $Li_{0.89}$ to match the cathode potential after formation cycling of the full cell. A salient feature of the present model is the rate-dependent diffusion coefficient D for Li^+ ions in the lithiated graphite, which is the same for all Li_xC_6 phases.[21] At 30 °C, this coefficient is given heuristically by

$$D = D_0(1 + a/(1 + I_0/I)),$$

where $a \approx 0.49$, the low-current diffusivity $D_0 \approx 9 \times 10^{12}$ cm^2 s^{-1}, and the threshold current density I_0 is 2.5C.

Results and Discussion

Constant current capacity limited charging.—Figures 2a and 2b show the cell voltage U plotted vs the specific capacity Q for different C-rates at 30 °C and 45 °C, respectively; the 37 °C and 55 °C data are shown in Fig. S2. These figures show that cell polarization increases as the rate increases; furthermore, this polarization is weaker at a higher temperature. During the 1 h rest, the cell voltage decreases to ~3.7 V at both temperatures, indicating that the open circuit potential changes only slightly with temperature. Regardless of the charge rate, the discharge plots lie on top of each other and the discharge capacities (after the 3 V hold) are similar to the charge capacities.

The individual electrode reference potentials are shown in Figs. 3a to 3d. At all test temperatures, the cathode accounts for a major portion of the cell polarization. For both electrodes, the electrode polarization is weaker at the higher temperature. As seen from Figs. 3a and 3b, the end-of-charge anode potential ϕ_a steadily decreases with the C-rate, eventually crossing zero; by polynomial interpolation in Fig. 4a, this crossing corresponds to 3.46C at 30 °C and 4.64C at 45 °C. For higher rates, charge capacity needs to be lowered to keep ϕ_a positive; the resulting "safe line" is shown in Fig. 4b. For a fixed C-rate, the specific charge capacity Q needs to be below this line to avoid Li plating. Comparing the 30 °C and 45 °C plots in Figs. 4a and 4b, one can see that while the anode polarization decreases at the higher temperature, the effect of this decrease is moderate, allowing only 1.2C increase in the "safe" C-rate.

Relaxation kinetics for the cell voltage after capacity limited charge are complex; there is a fast exponential component (of several tens of seconds) that is well accounted for by diffusional controlled ion transport in the electrolyte and the electrodes, but there is also a slow dispersive component that can be described by a stretched exponential covering 2–3 decades in time.[9] These behaviors are also seen in Figs. 5a and 5b. The relaxation kinetics after capacity limited charge at 30 °C are dispersive and bimodal. These features are also observed at 45 °C; in particular, there is a slow dispersive component seen after 1 min expanding over several decades in time. The time constants for this component weakly depend on the temperature (Figs. 5a and 5b), which is the case for other Kohlrausch kinetics.[22] The stretched exponential kinetics can be thought of as a continuum of first order kinetics; when the temperature increases, *all* such kinetics become accelerated, and the overall response may not change dramatically, as these contributions *all* shift to an earlier decade.[22–24] Kinetics for the electrode potentials follow the same trends as the cell voltage, but they also show additional features (see Figs. 5c and 5d and Figs. S3 and S4)

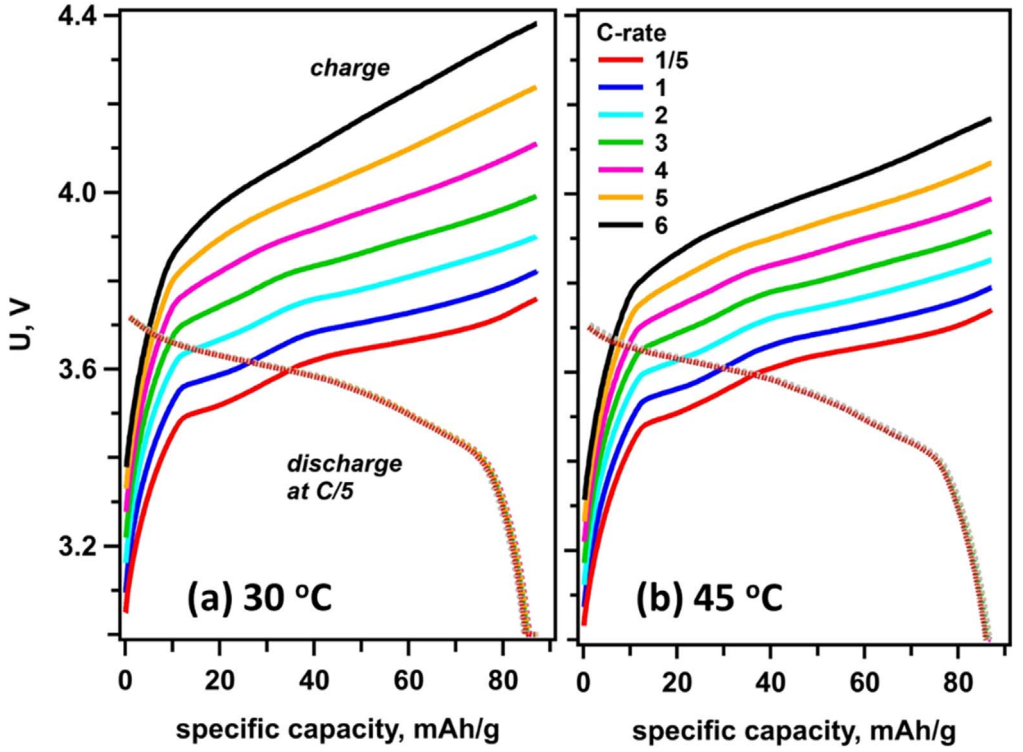

Figure 2. The cell voltage U vs specific capacity Q for constant current charging of the full cell from 3 V to a fixed capacity of 87 mAh g^{-1} at (a) 30 °C and (b) 45 °C. The lines of different color correspond to different C-rates given in the legend in panel b (1C = 1.97 mA cm^{-2}). After charge, the cells rest for 1 h at zero current and are then discharged to 3 V at a C/5 rate (dashed lines).

complicating their analyses. A positive ϕ_a maximum is attained at a delay time of 1–10 min. We had previously speculated that this feature could be related to Li plating.[8] As seen in Fig. 5d, at 45 °C this feature is seen even for charging currents that are too low for ϕ_a to become negative; this observation suggests that the feature is *not* related to Li plating. Explaining this feature remains a challenge as it is not replicated in our electrochemical model.

Pulse current charging terminated when ϕ_a = 0.—As stated earlier, the rectangular current pulses were applied at 3.57 V and the $\phi_a = 0$ termination condition was implemented by continuously monitoring the anode reference potential. This approach is illustrated in Fig. 6, which shows the anode potentials as a function of C-rate at different times during the pulse. The data can be used to quantify electrical resistivity of the cell and electrodes. The differences in cell voltage (or electrode potentials) divided by the peak current and multiplied by the electrode area gives the instant area specific impedance (ASI). Animated plots of the cell voltage, anode potentials, and instantaneous ASI during the pulse are shown in Figs. S5 and S6.

Figure 7, panels a to d show time evolution of the anode and cathode ASI during the pulsed charge. Because these pulses are terminated when ϕ_a reaches zero, the higher current pulses have shorter duration. Observe that the typical response includes a rapid initial (<10 ms) rise, which we term the Ohmic portion, followed by a gradual increase that is controlled by diffusion and Faradaic processes in the electrodes. As seen earlier, the Ohmic portion is consistently higher for the cathode; additionally, the ASI is lower at

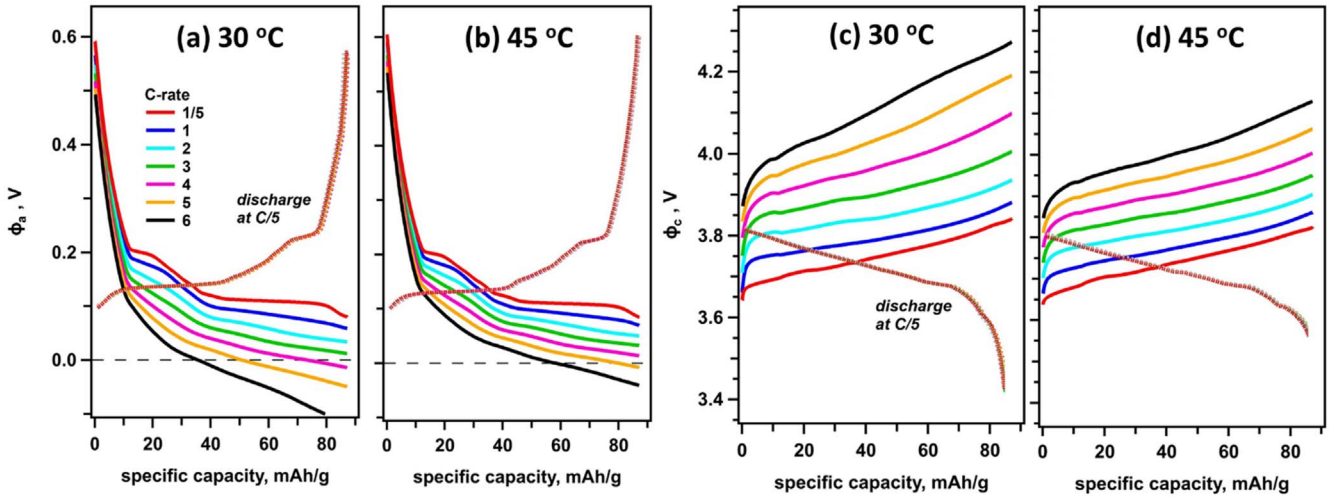

Figure 3. Like Fig. 2, for the (a), (b) anode and (c), (d) cathode reference potentials ϕ_a and ϕ_c, respectively, at 30 °C and 45 °C, as indicated in the plots.

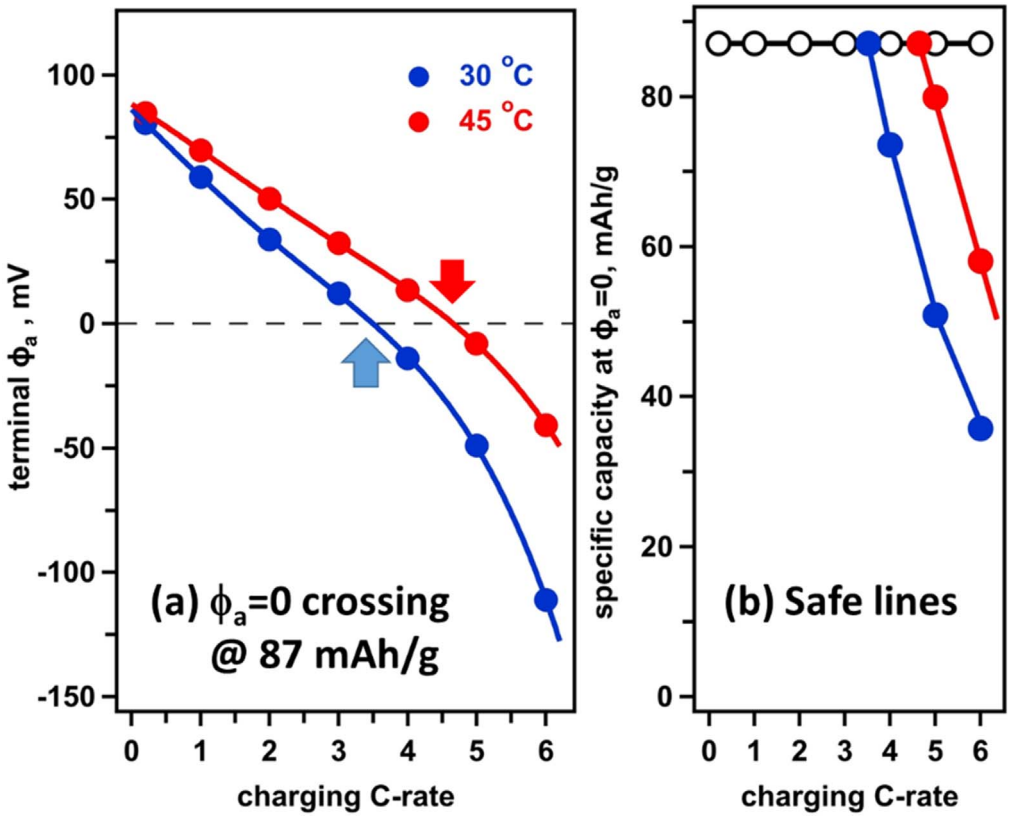

Figure 4. (a) The anode reference potential ϕ_a at 30 °C (*blue circles*) and 45 °C (*red circles*) at the end of a constant current 87 mAh g^{-1} charge at the specified C-rates. The solid lines are polynominal interpolation of the data. The crossing points indicated with the arrows correspond to the maximum C-rate at which ϕ_a is non-negative. (b) The "safe lines" (*color lines and filled circles*) for the two temperatures. The symbols correspond to the capacities at which $\phi_a = 0$ for a given constant current C-rate. The open circles give the terminal capacity. Staying below these lines avoids Li plating during fast charging of the cell.

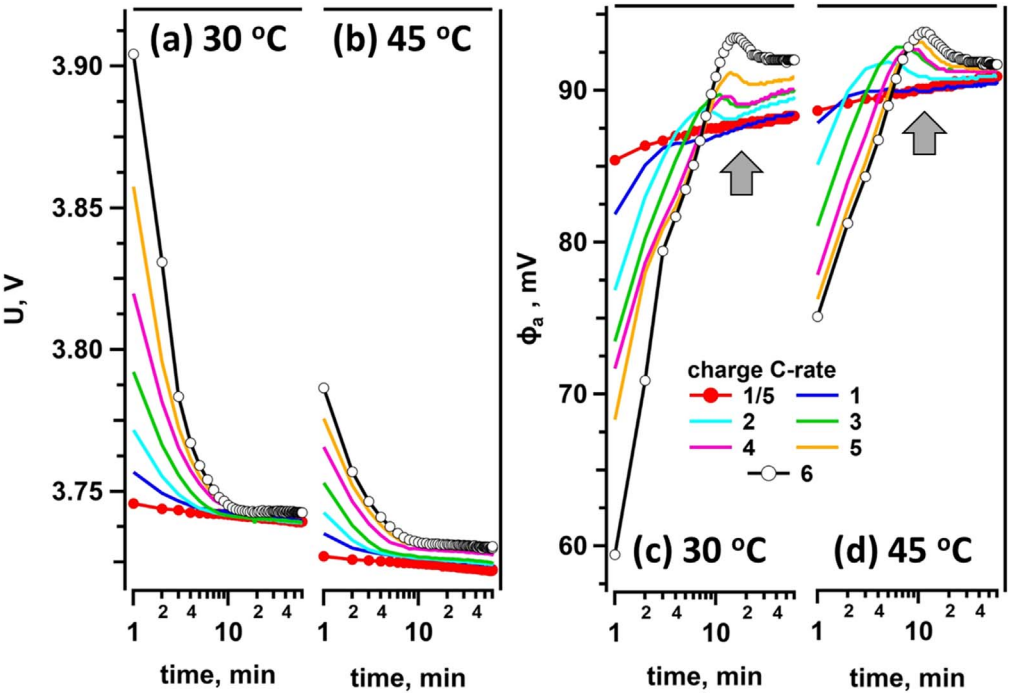

Figure 5. Relaxation kinetics observed at 30 °C and 45 °C for (a), (b) the cell voltage U and (c), (d) the anode reference potential ϕ_a after 87 mAh g^{-1} charge. Only the slow components of these kinetics (>1 min) are shown. In panel b, the arrows indicate the maxima in the plots.

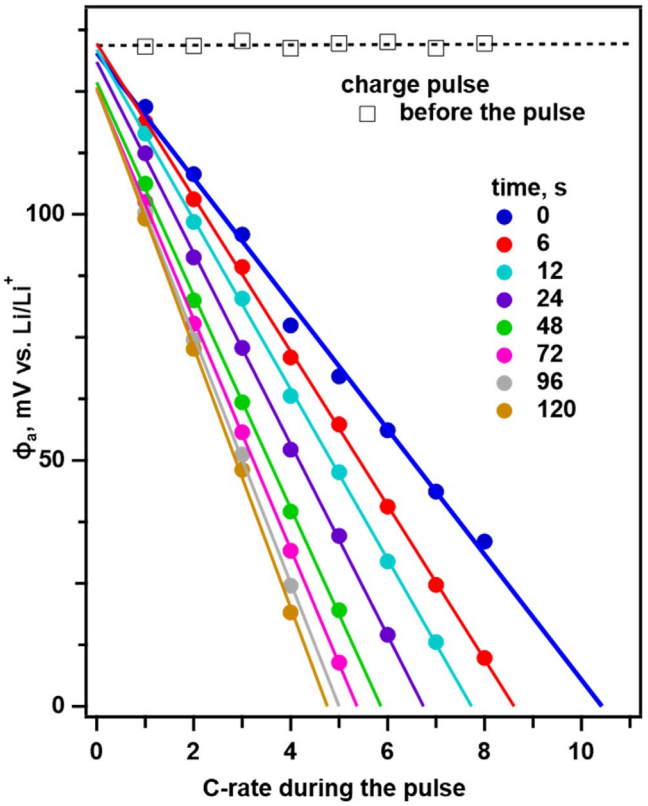

Figure 6. The anode reference potential at different delay times (*see the legend*) during a 120 s charge pulse applied at 3.57 V and 30 °C plotted vs the C-rate (*filled circles*). The straight lines are the least squares linear fits. The intersections of these lines with the *x*-axis give the critical C-rates for $\phi_a = 0$ crossing. The t = 0 data are obtained ~0.04 s after application of the current pulse and reflect the Ohmic potential drop, which increases with increasing C-rate; the gradual potential decrease that follows is governed by diffusional and Faradaic processes in the graphite anode.

45 °C, due to faster Li^+ diffusion at the higher temperature. For the cathode, all ASI kinetics line up (more so at 30 °C than at 45 °C, see Figs. 7b and 7d). For the graphite anode (Figs. 7a and 7c), the kinetics match over the first 30 s and then increasingly diverge, with the higher currents giving the lower impedances. This divergence becomes even more visible at 45 °C; for example, the instant ASI is lower at 4C than at 1C. Because of the $\phi_a = 0$ termination condition, the smaller ASI at 4C is *not* a consequence of Li plating on the graphite. In Ref. 21 we hypothesized that at high currents the diffusion of lithium in the LiC_x phases becomes increasingly faster. Indeed, lattice strain smearing of X-ray diffraction peaks in the LiC_x electrode during rapid charge (>1C) is seen (e.g.[25]), and the resulting defects can cause faster filling of layers between the graphene sheets; see Ref. 26 for other nonequilibrium phenomena that are involved.

Figures 8a and 8b show instant electrode ASI for the capacity limited (2.5 mAh g^{-1}) pulsed charging at 30 °C; similar plots are observed at the other temperatures. When the ASI is plotted vs time the kinetics line up; comparison of Figs. 7a and 8a indicates that the "lower instant ASI at higher C-rate" phenomenon is not evident for shorter pulse durations. This constant capacity pulse charging facilitates comparison of relaxation kinetics as shown in Fig. 9, panels a to d. The $U(t)$ and $\phi_a(t)$ plots start at different values due to cell and anode polarization, which is stronger at faster rates. At both temperatures, the $U(t)$ kinetics are bimodal with a short exponential component (<1 min) and a long tail; all traces converge to the same tail. The shape of the slow component does not change much with the temperature (Figs. 9a and 9c). The bimodality is also observed for the anode reference potential (Figs. 9b and 9d), but there is also a growing feature seen for the highest currents and more visible at the higher temperature (similar to the feature seen in Figs. 5c and 5d).

Earlier in Fig. 6 we showed that during a charge pulse, $\phi_a(t)$ decreases over time t, so for a sufficiently strong current I_p there is an instant of time t at which $\phi_a(t) = 0$. For short pulses, $\phi_a(t)$ at a fixed time delay t is almost linear with I_p, so by plotting $\phi_a(t)$ vs I_p we can extrapolate the former quantity to zero as shown in Fig. 6, and in this way estimate the crossing current I_p without passing through the crossing point. This linearly extrapolated crossing current I_p gives the critical transferred capacity $Q = tI_p$ at which the crossing occurs. The latter can be converted to the lithiation Δx transferred during the pulse from $\Delta x = Q/Q_{full}$. Figures 10a and 10b summarize the extrapolated crossing C-rates plotted vs the pulse duration and the transferred lithiation Δx. At 45 °C, the crossing currents are significantly higher compared to 30 °C, so there are tangible gains in "safe" pulsed charging at the higher temperature.

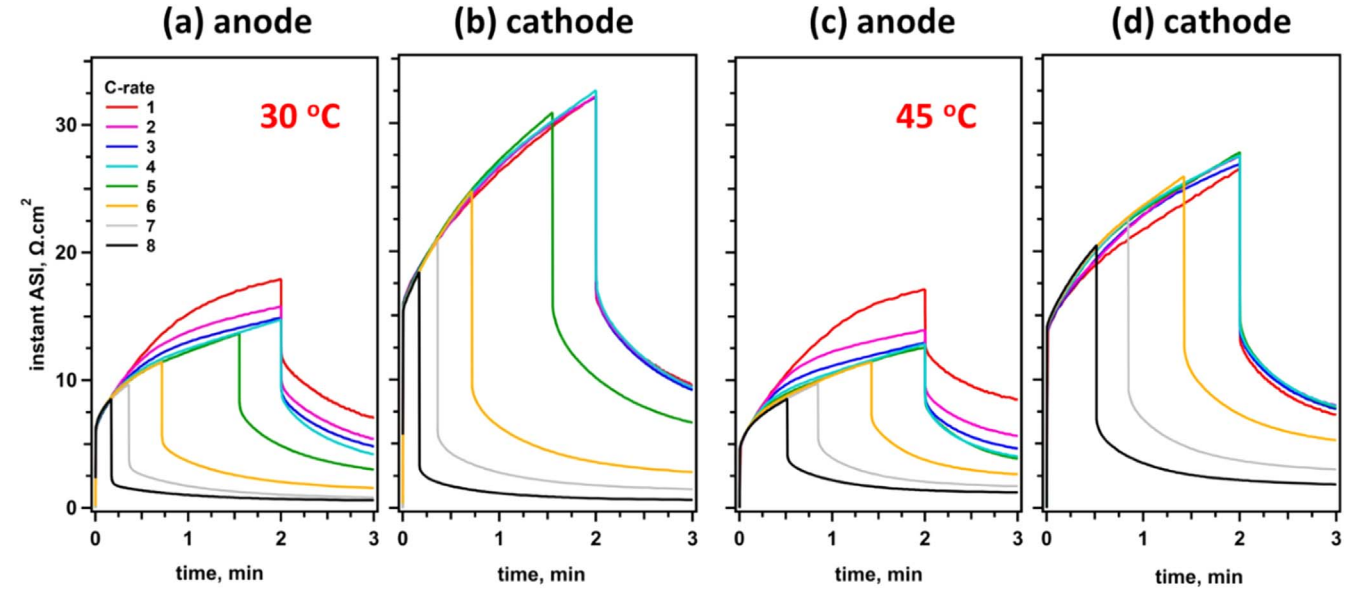

Figure 7. The instant ASI for pulsed charging of a cell from 3.57 V at (a), (b) 30 °C and (c), (d) 45 °C. The anode (a), (c) and cathode (b), (d) contributions are shown separately. The pulse is 120 s long unless the $\phi_a = 0$ condition is met. While for the cathode the kinetics for different C-rates are similar, for the lithiated graphite anode there is an increasing divergence over time, especially at 45 °C.

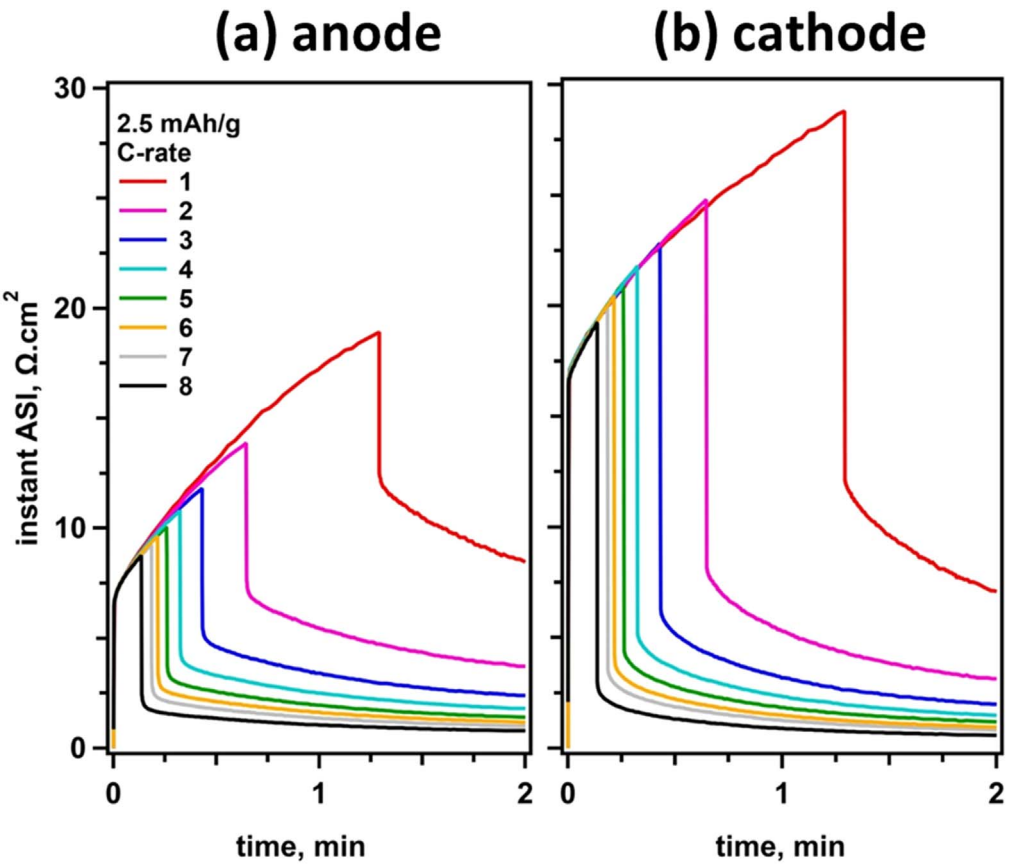

Figure 8. The same as Figs. 7a and 7b, for the constant capacity (2.5 mAh g^{-1}) pulses at 30 °C.

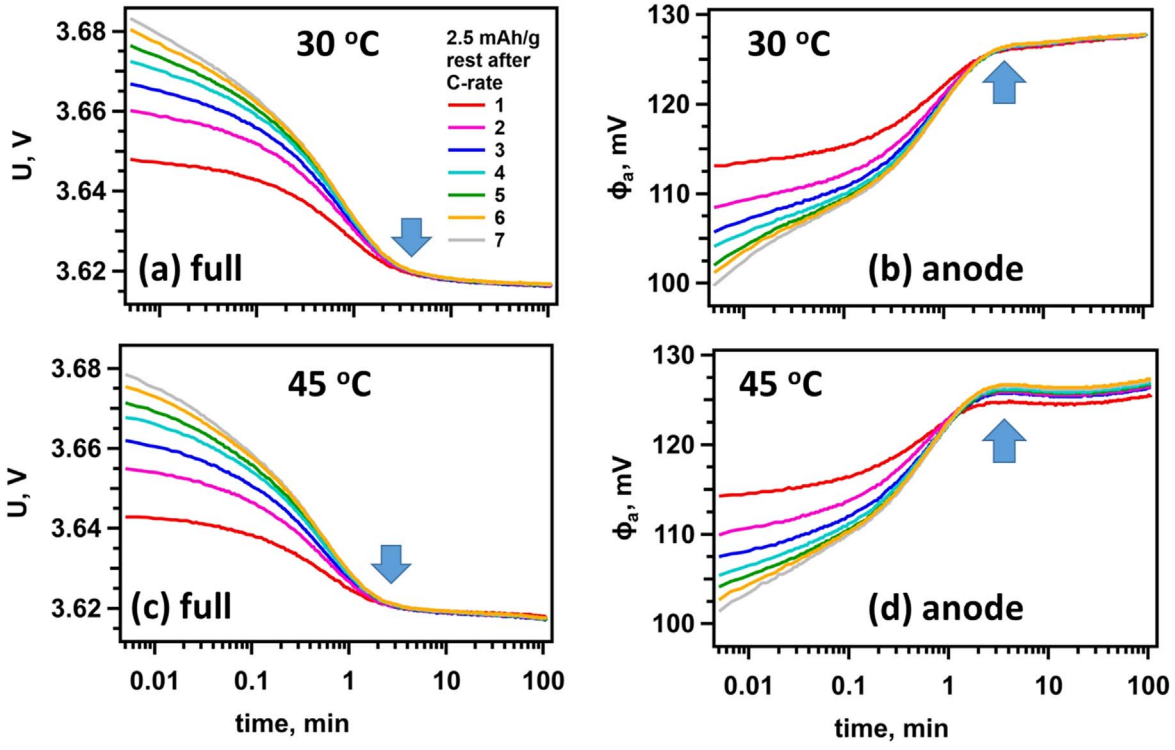

Figure 9. Relaxation kinetics of (a), (c) the cell voltage and (b), (d) the anode reference potential observed after constant-capacity (2.5 mAh g^{-1}) charging of a cell at 3.57 V and (a), (b) 30 °C and (c), (d) 45 °C. Both families show a fast exponential decay within the first minute followed by a slow decay on a longer time scale. Note convergence of the traces obtained for different C-rate (indicated in panel a) in the full cell data (*arrows on the left*). The anode potential shows more variation, with the "bump" (*see arrows on the right*) seen more clearly at a higher temperature. The same feature is observed when the current is abruptly stopped after a long constant current charging of a cell (see Figs. 5c and 5d).

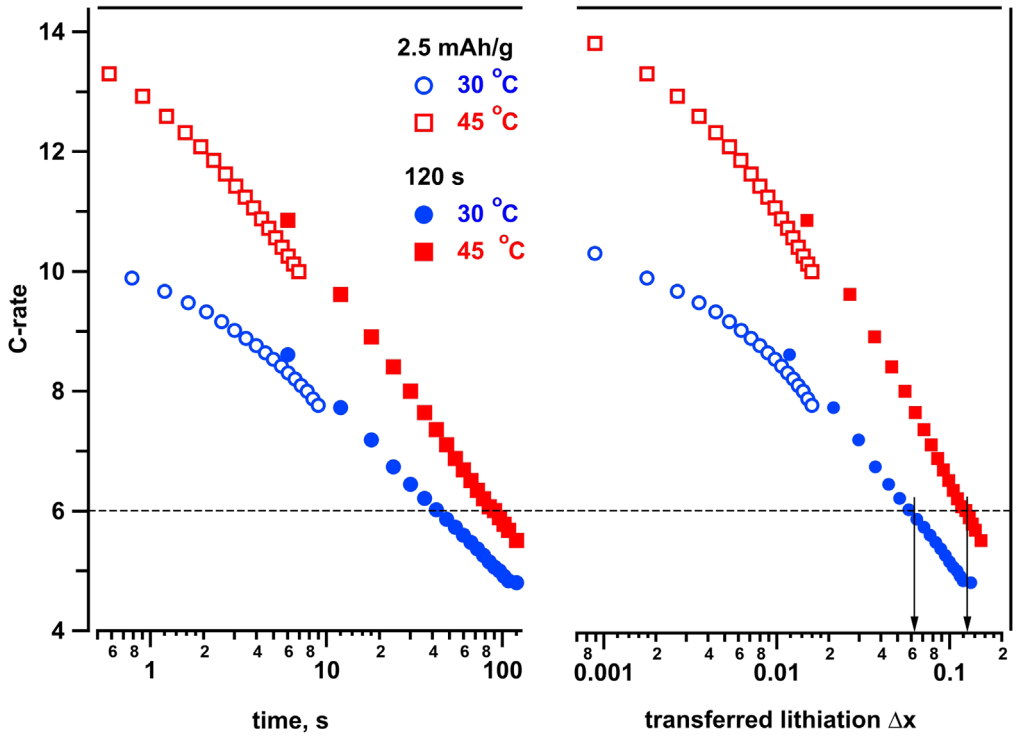

Figure 10. The "safe lines" for pulsed charging of a cell at 3.57 V at the indicated temperatures. The symbols give the extrapolated currents corresponding to the $\phi_a = 0$ crossings at fixed (a) pulse duration or (b) Li fraction Δx transferred from the oxide cathode by the pulse. Staying below these lines prevents Li plating in the cell. The horizontal dashed line corresponds to a rate of 6C; the vertical arrows indicate Δx for $\phi_a = 0$ condition. The plot combines the constant-capacity (2.5 mAh g^{-1}) and constant duration (up to 120 s) measurements.

To illustrate, for 6C the safe capacities transferred by the pulse are 8.5 mAh g^{-1} at 30 °C vs 17.2 mAh g^{-1} at 45 °C; i.e., twice as much charge can be transferred by a 6C pulse without reaching the $\phi_a = 0$ condition.

Performance degradation from exposure to high temperatures.—Exposing LIBs to high temperatures is known to degrade cell performance. To better characterize this effect, we measured the capacity and impedance of our cells at 30 °C, before and after conducting the constant current and pulse current measurements at the set temperatures over a ~95 h period (see Fig. S1). Representative data are shown in Table I and Fig. S7. The cells showed small capacity losses, which were similar at 30 °C, 37 °C, 45 °C (~6%), but slightly higher (~7.7%) at 55 °C (Table I). Cell impedance also increased during the measurement (Table I), with the increase being greater at the higher temperatures and especially noticeable at 55 °C. For example, ASIs at a cell voltage of 3.85 V increased by 5.5 %, 12.0 %, 15.1 % and 38.5% at the temperatures of 30 °C, 37 °C, 45 °C and 55 °C, respectively. Most of this ASI rise occurs at the cathode (Fig. S7) and could be the result of increased oxide particle cracking and crystallographic changes, especially at the oxide surface.[27,28,29]

Electrochemical modeling.—Before delving into the results of cell modeling, we revisit the points shown in Fig. 1: ***CC*** and ***CA*** are the surfaces of the cathode and the anode, respectively, at the corresponding current collectors, ***R*** is the middle plane of the separator (where the reference electrode is placed), and ***SC*** and ***SA*** are the electrode surfaces contacting the separator.

Let $\phi_{1,2}(z)$ be the potentials in the solid electrodes (index 1) and liquid electrolyte (index 2) at the cell depth z. Then the reference potentials for the cathode and anode vs Li/Li^+ are given by $\phi_c = \phi_1(CC) - \phi_2(R)$ and $\phi_a = \phi_1(CA) - \phi_2(R)$ respectively, and the cell voltage $U = \phi_c + \phi_a$. What matters for Li plating is not the anode reference potential ϕ_a as such, but the Li plating overpotential η given by the difference between the electrode and electrolyte potentials at the interface. This quantity is minimum at the electrode/separator interface. Due to high conductivity of the anode matrix, we can assume that $\phi_1(CA) \approx \phi_1(SA)$ (the differences computed in our electrochemical models are <1.5 mV). Thus, considering the worst case, which is at ***SA***, charging to avoid Li plating should be such that the overpotential $\eta_a = \phi_1(CA) - \phi_2(SA) > 0$. Note that this overpotential is the same as the anode *surface* potential vs Li/Li^+.[30] The Li plating overpotential increases with the depth z across the graphite electrode, so $\eta_a > 0$ ensures avoidance of the thermodynamic Li plating condition (LPC) in the entire anode.[6]

During charge η_a is greater than ϕ_a by $\Delta\phi_a = \phi_2(SA) - \phi_2(R)$, which is the positive potential drop in the electrolyte across the separator. This quantity decreases with increasing temperature and increases with increasing separator thickness and porosity; it also increases linearly with the current. For our 20 μm thick Celgard 2320 separator infused with 1.2 M $LiPF_6$ in a carbonate solvent, $\Delta\phi_a$ increases by ≈4.7 mV per 1C at 30 °C, so for 6–8C rate, there is a considerable offset. For this reason, stopping fast charge when $\phi_a = 0$ (which is implemented experimentally in this study) *terminates lithiation of graphite before the LPC of* $\eta_a \leqslant 0$ *is reached*. As detailed above, our approach in this study is first to map the charging regimes for which $\phi_a = 0$ condition is met. We use this input to adjust the model parameters to replicate these boundaries (which are referred to as the "safe lines"), and then use an electrochemical model to predict charging conditions at which $\eta_a = 0$ occurs. In this way, what is impossible through experimentation alone becomes possible through parameter adjustment and model predictions.

For the constant-current charging, the typical simulation of η_a vs Q plots for 70 μm thick, 30 °C cell is shown in Fig. 11a, with the transferred lithiation x at the crossing current shown in Fig. 11b (which extrapolates Fig. 4b). Note that the crossing currents are calculated for the anode reference and surface potentials in a cell with two standard separators, as in our reference electrode experiments. Figures 12a and 12b extend these results for cells with different electrode thicknesses (assumed to be the same for both

Table I. Capacity fade and end-of-pulse ASI at 30 °C, before and after the high-rate tests.

T, °C	Discharge capacity fade, % [a)]	Full cell ASI, Ω.cm^2 [b)]	change, % [c)]	Cathode ASI, Ω.cm^2 [b)]	change, % [c)]	Anode ASI, Ω.cm^2 [b)]	change, % [c)]
30	5.2	25.0	5.5	17.0	6.9	8.0	3.1
37	6.1	25.0	12.0	16.6	14.5	8.5	6.1
45	5.9	23.7	15.1	15.8	20.9	8.0	3.4
55	7.7	24.1	38.5	16.0	48.7	8.0	18.5

a) Cell discharge capacity fade at a C/25 rate (3–4.1 V cycling) and 30 °C; the temperatures are given for cell aging during a ∼95 h test period. b) End-of-pulse ASI for 10 s, 3C pulse determined at ∼3.85 V prior to the high-current tests in Fig. S1. c) Relative change in the ASI after the test (also see Fig. S7).

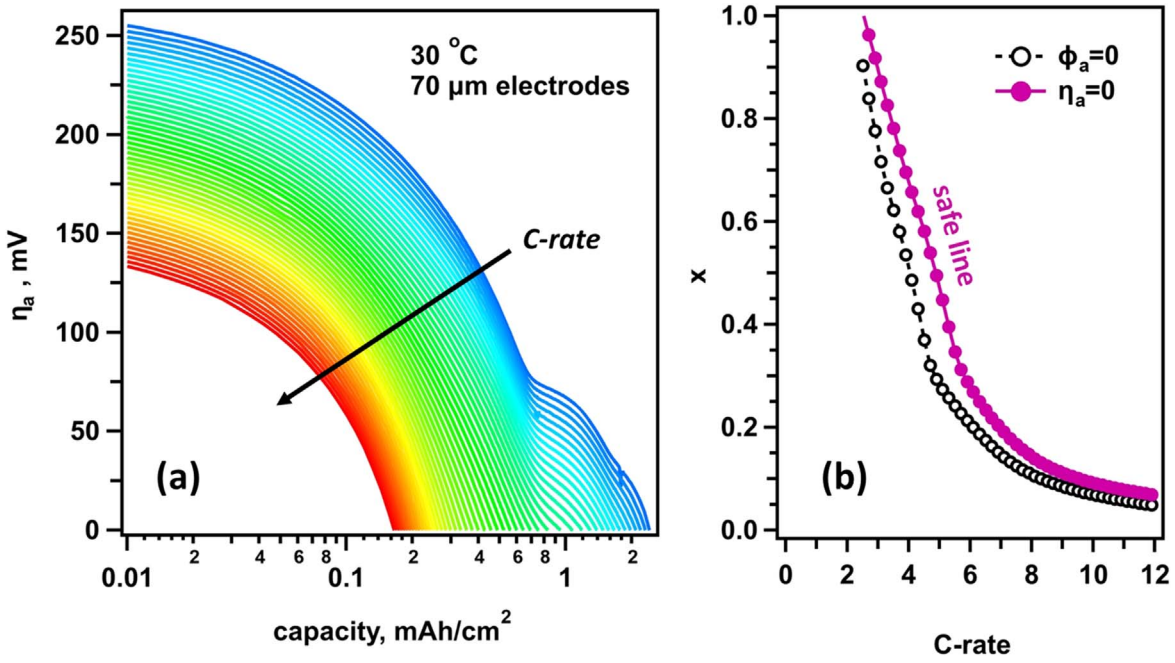

Figure 11. (a) Simulated plots of the anode surface potential η_a vs the area specific lithiation capacity for 70 μm thick electrodes at 30 °C. The color progresses from blue to red in the rainbow order as the C-rate increases. (b) The transferred lithiation corresponding to the capacities at which the anode reference (*open circles, dashed line*) and surface (*filled circles, solid line*) potentials reach zero are plotted as a function of the C-rate. The initial decrease is linear, but then the dependence becomes curved. The solid trace gives the "safe line" for constant current charging at each rate. The C-rates in panel b correspond to the color traces in panel a.

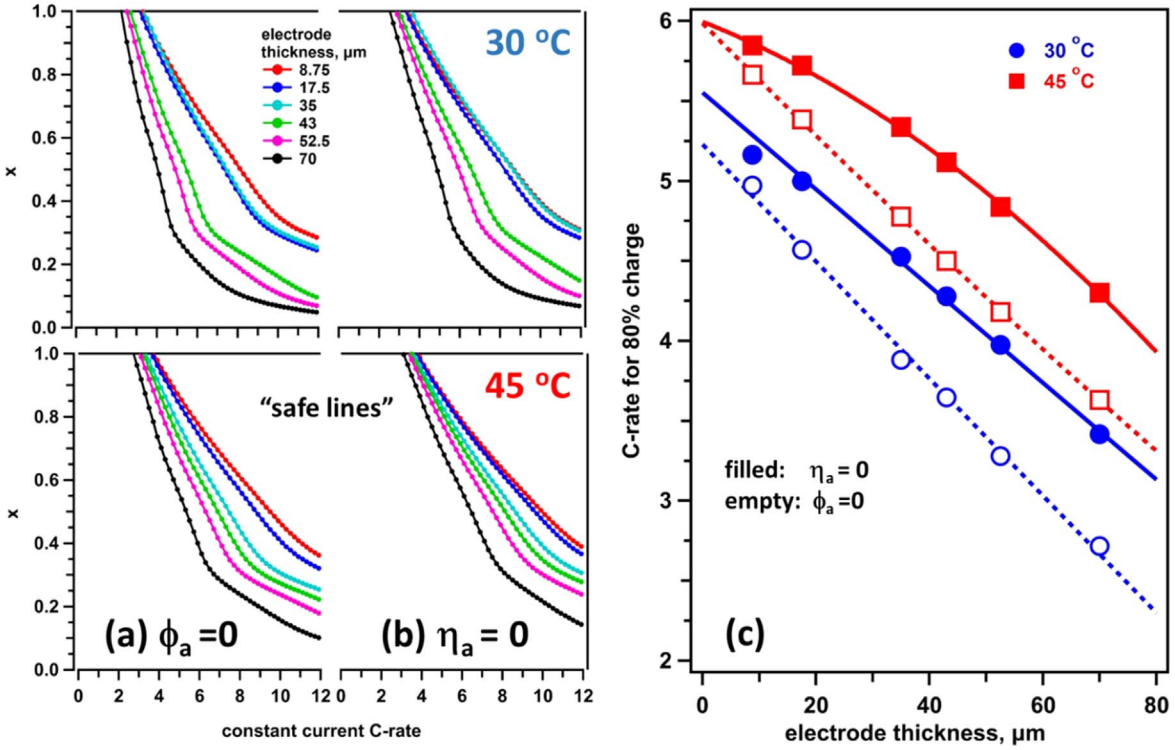

Figure 12. (a), (b) The "safe lines" computed for cells with different electrode thicknesses in which the transferred lithiations x for achieving (a) $\phi_a = 0$ or (b) $\eta_a = 0$ are plotted vs the C-rate of constant current for 30 °C and 45 °C. Staying below the "safe lines" in panel b helps avoid Li plating during fast charge. (c) A crosscut of these plots at 80% full charge, with the critical C-rates plotted vs the electrode thickness. The blue lines and symbols are for 30 °C and the red ones are for 45 °C. The filled circles and solid lines are for $\eta_a = 0$ and the empty circles and dashed lines are for $\phi_a = 0$ (these two conditions become the same for an infinitely thin separator). Achieving a *constant current* charge rate of 6C without Li plating would be impossible for these cells even for very thin electrodes; for 70 μm thick electrodes, Li-plating would not occur with a 4C charge rate at 45 °C.

electrodes). For the C-rates below 6C the "safe lines" in Fig. 12a are nearly straight, as in our experiment (Fig. 4b), but for thicker electrodes they bend up above 6C. Using this plot, one can find what C-rate is "safe" for a given transferred lithiation x during charge. E.g., using $\eta_a = 0$ as a guide for the onset of LPC, for 6C charge at 45 °C, only 56% of the full cell capacity can be "safely" reached for

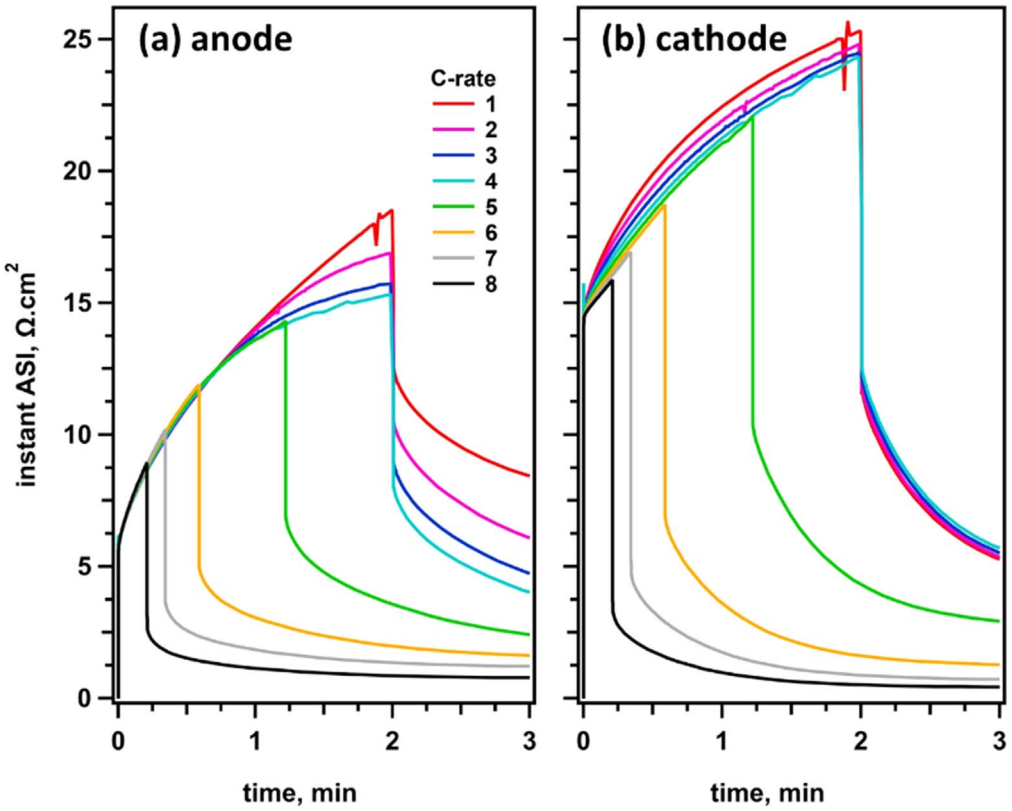

Figure 13. A numerical simulation of the kinetic data for ASI (at 30 °C) shown in Figs. 7a and 7b using our electrochemical model. In this model, the increasing divergence of the anode kinetics for different C-rates originates through a rate dependent lithium diffusivity in the LiC_x electrode.

70 μm thick electrodes and 73% for 35 μm electrodes. According to these calculations, obtaining 80% capacity at 6C, while avoiding LPC would require electrodes thinner than 9 μm.

Figure 12c shows the maximum C-rate at which 80% charge can be achieved while maintaining non-negative reference or surface anode potentials. The 6C rate of constant current charging cannot be achieved without meeting LPC at either temperature, while 5C can be achieved using electrodes thinner than 20 μm at 30 °C and 50 μm at 45 °C; 4C can be achieved using electrodes thinner than 52 μm at 30 °C and 76 μm at 45 °C. As explained above, further increase in the temperature is counterproductive as the increased resistance due to cell aging offsets the gains from faster diffusion.

To model the pulse current charging, a 120 s long charge pulse was applied at 3.57 V, and the pulse was terminated when ϕ_a or η_a reached zero. This voltage was chosen so that even at the highest C-rate the cathode potential remained sufficiently low to avoid oxidation of electrolyte. Figures 13a and 13b show the simulated ASI kinetics at 30 °C that can be compared with the experimental traces shown in Figs. 7a and 7b. As in the latter plots, the anode ASI kinetics increasingly diverge over time for delay times >1 min (Fig. 13a) whereas for the cathode (Fig. 13b) the divergence is relatively small (cf. Fig. 7b). In our model these behaviors originate through the rate-dependent Li diffusion in graphite, so the implication of the experimental data is that *lithium migration in the LiC_x electrode accelerates significantly at high rates when the graphite lattice becomes strained.* It was impossible to model the fast charge regimes without taking this effect into account.

Figures 14a and 14b present simulations of the "safe lines" in Figures 10a and 10b. Using the model, we calculated the "safe line" for the anode *surface* potential η_a which is not accessible experimentally. As seen from the plot, due to potential drop across the electrolyte-filled separator, the difference between the crossing currents corresponding to these anode potentials systematically increases with the current rate. The overall shape of these "safe lines" compare well with the experimental data shown in Figures 10a and 10b. As the correction in the potential comes mainly from the electrolyte (Fig. 1), we have reasonable confidence that the "safe line" for $\eta_a = 0$ in Figs. 14a and 14b is accurate, and elsewhere we use it to prescribe pulse sequences that avoid LPC while providing an average charge rate, well in excess of 4C, that precludes Li-plating.

Conclusions

Constant current and pulse current charging were conducted on NCM523/Gr cells containing a Li-metal reference electrode at 30 °C, 37 °C, 45 °C, and 55 °C. By repeating the experiment for many C-rates we mapped the currents at which the anode potential (as measured by the reference electrode) reached or crossed zero vs Li/Li^+. We used these maps, and a state-of-the art multiphase electrochemical model, to compute the currents at which anode *surface* potential reaches zero vs Li/Li^+, thereby determining the boundary of charging regimes that cause Li plating on the graphite anode. The highlights from the experimental data and model simulations are as follows:

1. Generally, the cell and electrode polarization at faster charge decreases with increasing test temperature. At all temperatures, polarization at the oxide cathode is considerably greater than polarization at the graphite anode. However, at temperatures >45 °C the gains through speeding of Li^+ ion diffusion become offset by growing resistance, especially at the oxide-cathode. Thus, increasing temperature over 45 °C for extended periods is counter-productive because it degrades long-term cell performance.
2. For constant current charge, higher capacities can be "safely" attained (meaning no Li plating on the graphite anode) with lower C-rates, thinner electrodes, and higher temperatures (see Fig. 12). For a 70 μm thick electrode, full cell capacity can

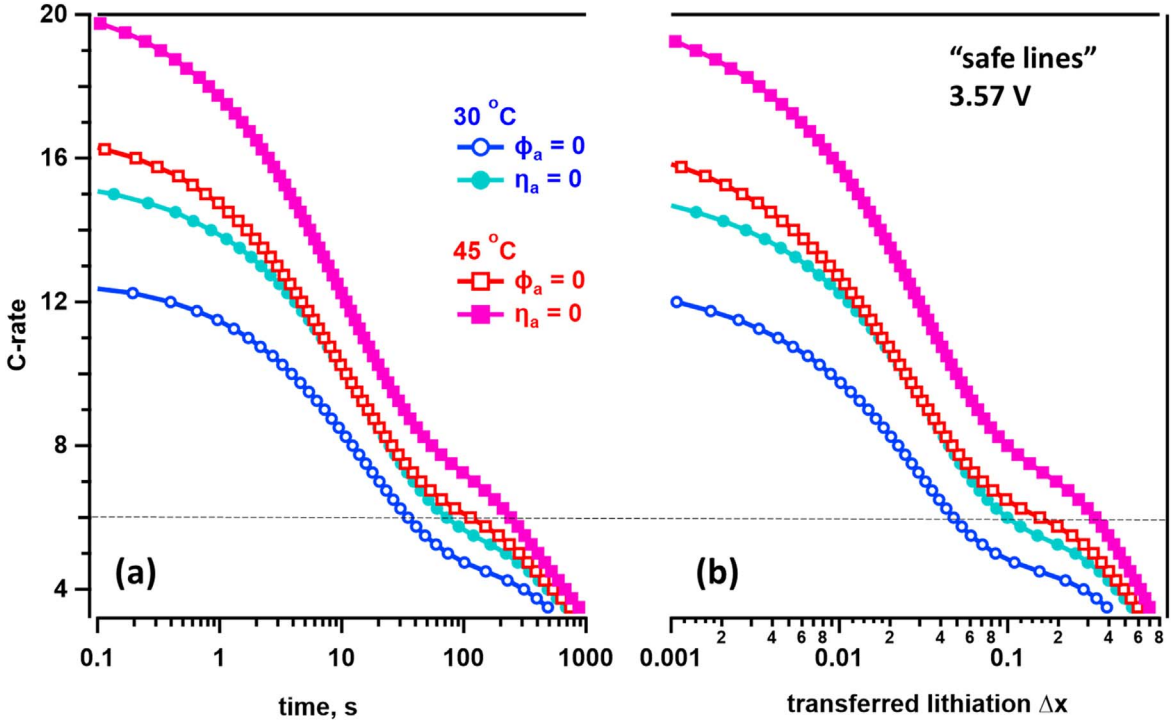

Figure 14. A numerical simulation of the "safe lines" shown in Fig. 10 plotted over an extended range in both axes. The crossing (a) times and (b) lithiation x transferred by a rectangular pulse applied at 3.57 V are plotted vs the charge C-rate (*the vertical axis*). The empty and filled symbols are for the anode reference and surface potentials, respectively, for 30 °C (*circles*) and 45 °C (*squares*). The difference between the two potentials increases with the C-rate. For a fixed time/lithiation, the C-rates below the $\eta_a = 0$ lines guarantee a positive Li plating overpotential.

be achieved with a 3C rate at 45 °C, whereas only 56% of the capacity can be reached at a 6C rate. In contrast, only 25% capacity can be achieved at 30 °C at this rate.

3. For pulsed charge, the likelihood of Li plating increases considerably with increasing rate and duration of the pulse but decreases with the increasing temperature (see Fig. 14). We give the general methodology of obtaining the "safe lines" for different charge regimes without crossing into the Li plating "danger zone" during the measurement. This allows mapping of the boundaries in rich detail.
4. At all temperatures, cell relaxation displays stretched exponential (Kohlrausch) kinetics, which includes a fast exponential component and a slow dispersive component extending over several decades in time. The electrode potentials generally follow the cell voltage trends, except for a maxima seen in the anode potentials after ~10–20 min of rest, which appears earlier at the higher temperatures.

According to these results, fast charging at high temperatures lessens the risk of Li plating. However, prolonged exposure to temperatures over 45 °C should be avoided as it increases the positive electrode (and cell) impedance. Even at this temperature attaining a constant 6C charge to 80% full capacity is untenable for all but the thinnest electrodes. High temperature, by itself, is not enough to enable extreme fast charging: higher conductivity electrolytes, lower tortuosity electrodes and faster electrode-electrolyte interfaces are needed. Our pulsed charge experiments indicate that faster average charging can be achieved by continuous adjustment of the current so that the anode surface potential remains slightly above zero vs Li/Li^+ during charge.[6] The data and simulations in this manuscript are for cells containing two separators and a reference electrode. We are developing methodologies to apply these ideas in practical cells contain a single separator; these approaches will be experimentally demonstrated in upcoming articles.

Acknowledgments

Funding was provided by the U.S. DOE Office of Vehicle Technology Extreme Fast Charge Cell Evaluation of Lithium-Ion Batteries (XCEL) Program managed by Samuel Gillard. Support from the U.S. DOE's Office of Vehicle Technologies is gratefully acknowledged. The electrodes used in this article are from Argonne's Cell Analysis, Modeling and Prototyping (CAMP) Facility, which is fully supported by the DOE Vehicle Technologies Office (VTO). We are grateful to our many colleagues (Dennis Dees, Stephen Trask, Bryant Polzin, Andrew Jansen and Kandler Smith) for their support during this work. The submitted manuscript has been created by UChicago Argonne, LLC, Operator of Argonne National Laboratory ("Argonne"). Argonne, a U.S. Department of Energy Office of Science laboratory, is operated under Contract No. DE-AC02-06CH11357. The U.S. Government retains for itself, and others acting on its behalf, a paid-up nonexclusive, irrevocable worldwide license in said article to reproduce, prepare derivative works, distribute copies to the public, and perform publicly and display publicly, by or on behalf of the Government. This work was authored in part by the National Renewable Energy Laboratory, operated by Alliance for Sustainable Energy, LLC, for the U.S. Department of Energy (DOE) under Contract No. DE-AC36-08GO28308. The views expressed in the article do not necessarily represent the views of the DOE or the U.S. Government.

ORCID

Marco-Tulio F. Rodrigues https://orcid.org/0000-0003-0833-6556
Ilya A. Shkrob https://orcid.org/0000-0002-8851-8220
Andrew M. Colclasure https://orcid.org/0000-0002-9574-5106
Daniel P. Abraham https://orcid.org/0000-0003-0402-9620

References

1. C. Michelbacher et al., *J. Power Sources*, **367**, 214 (2017).
2. M. Keyser et al., *J. Power Sources*, **367**, 228 (2017).

3. T. R. Tanim et al., *J. Electrochem. Soc.*, **166**, A1926 (2019).
4. A. Mistry, F. L. E. Usseglio-Viretta, A. Colclasure, K. Smith, and P. P. Mukherjee, *J. Electrochem. Soc.*, **167**, 090542 (2020).
5. E. J. McShane, A. M. Colclasure, D. E. Brown, Z. M. Konz, K. Smith, and B. D. McCloskey, *ACS Energy Lett.*, **5**, 2045 (2020).
6. W. Mai, A. M. Colclasure, and K. Smith, *J. Electrochem. Soc.*, **167**, 080517 (2020).
7. M.-T. F. Rodrigues, K. Kalaga, S. E. Trask, D. W. Dees, I. A. Shkrob, and D. P. Abraham, *J. Electrochem. Soc.*, **166**, A996 (2019).
8. I. A. Shkrob, M.-T. F. Rodrigues, D. W. Dees, and D. P. Abraham, *J. Electrochem. Soc.*, **166**, A3305 (2019).
9. I. A. Shkrob, M.-T. F. Rodrigues, and D. P. Abraham, *J. Electrochem. Soc.*, **166**, A4168 (2019).
10. M. Petzl and M. A. Danzer, *J. Power Sources*, **254**, 80 (2014).
11. J. C. Burns, D. A. Stevens, and J. R. Dahn, *J. Electrochem. Soc.*, **162**, A959 (2015).
12. C. v. Lüders, V. Zinth, S. V. Erhard, P. J. Osswald, M. Hofmann, R. Gilles, and A. Jossen, *J. Power Sources*, **342**, 17 (2017).
13. I. D. Campbell, M. Marzook, M. Marinescu, and G. J. Offer, *J. Electrochem. Soc.*, **166**, A725 (2019).
14. T. Waldmann, B.-I. Hogg, and M. Wohlfahrt-Mehrens, *J. Power Sources*, **384**, 107 (2018).
15. D. P. Abraham, E. M. Reynolds, P. L. Schultz, A. N. Jansen, and D. W. Dees, *J. Electrochem. Soc.*, **153**, A1610 (2006).
16. X.-G. Yang, T. Liu, Y. Gao, S. Ge, Y. Leng, D. Wang, and C.-Y. Wang, *Joule*, **3**, 3002 (2019).
17. J. A. Gilbert, J. Bareño, T. Spila, S. E. Trask, D. J. Miller, B. J. Polzin, A. N. Jansen, and D. P. Abraham, *J. Electrochem. Soc.*, **164**, A6054 (2017).
18. C. Peebles, J. Garcia, A. P. Tornheim, R. Sahore, J. Bareño, C. Liao, I. A. Shkrob, H. H. Iddir, and D. P. Abraham, *J. Phys. Chem. C*, **122**, 9811 (2018).
19. D. P. Abraham, D. W. Dees, J. Christophersen, C. Ho, and A. N. Jansen, *Int. J. Energy Res.*, **34**, 109 (2010).
20. K. G. Gallagher, D. W. Dees, A. N. Jansen, D. P. Abraham, and S.-H. Kang, *J. Electrochem. Soc.*, **159**, A2029 (2012).
21. D. W. Dees, M.-T. F. Rodrigues, K. Kalaga, S. E. Trask, I. A. Shkrob, D. P. Abraham, and A. N. Jansen, *J. Electrochem. Soc.*, **167**, 120528.
22. J. C. Phillips, *Rep. Prog. Phys.*, **59**, 1133 (1996).
23. E. Cuervo-Reyes and R. Flückiger, *J. Electrochem. Soc.*, **166**, A1463 (2019).
24. A. Plonka, *Progr. React. Kinet. Mechanism*, **25**, 109 (2000).
25. K. P. C. Yao, J. S. Okasinski, K. Kalaga, I. A. Shkrob, and D. P. Abraham, *Energy Environ. Sci.*, **12**, 656 (2019).
26. J. C. Garcia, I. Bloom, C. Johnson, D. Dees, and H. Iddir, *J. Phys. Chem. C*, **124**, 8162 (2020).
27. D. P. Abraham, R. D. Twesten, M. Balasubramanian, I. Petrov, J. McBreen, and K. Amine, *Electrochem. Comm.*, **4**, 620 (2002).
28. S. J. Harris and P. Lu, *J. Phys. Chem. C*, **117**, 648 (2013).
29. E. Hu, X. Wang, X. Yu, and X.-Q. Yang, *Acc. Chem. Res.*, **51**, 290 (2018).
30. P. Arora, M. Doyle, and R. E. White, *J. Electrochem. Soc.*, **146**, 3543 (1999).